Electronic Supplementary Material (ESI) for Journal of Materials Chemistry A.

Supporting Information

Bromomethylation of high-surface area carbons as a versatile synthon: Adjusting the electrode-electrolyte interface in lithium-sulfur batteries

Samuel J. Fretz[2], Christopher T. Lyons[1], Ella Levin[1], Christopher E. D. Chidsey[1], Anders E. C. Palmqvist[2], and T. Daniel P. Stack[1].

[1]Stanford University, Department of Chemistry, Stanford, California 94305, United States
[2]Chalmers University of Technology, Department of Chemistry and Chemical Engineering, SE-412 96 Gothenburg, Sweden

Figures for surface modifications

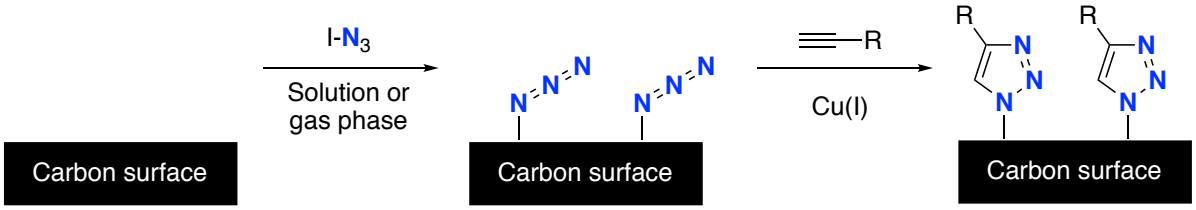

Figure S1. Two-step carbon functionalization scheme employing iodine azide (IN_3) to graft azide groups to the surface followed by coupling to a terminal alkyne using a Cu(I)-catalyzed azide-alkyne cycloaddition reaction.[1-3]

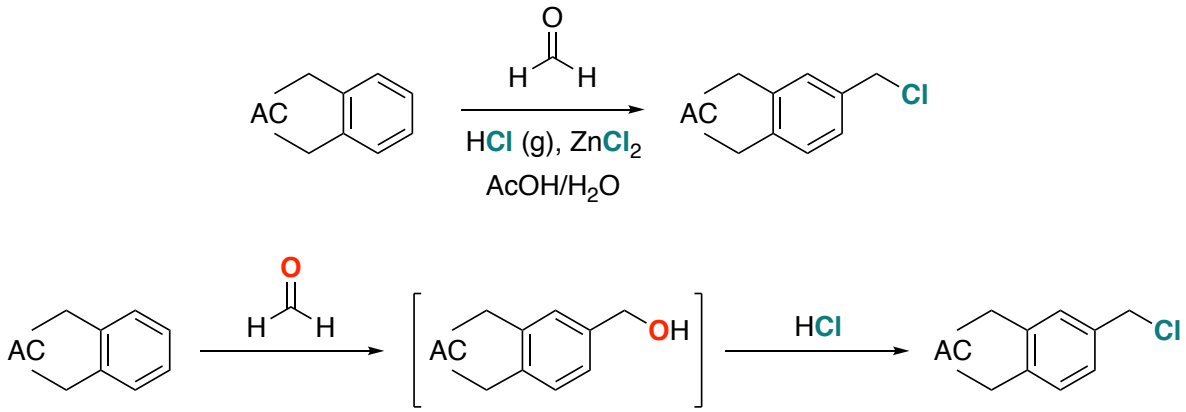

Figure S2. Chloromethylation reaction of AC (above) and its proposed mechanism (below).[4]

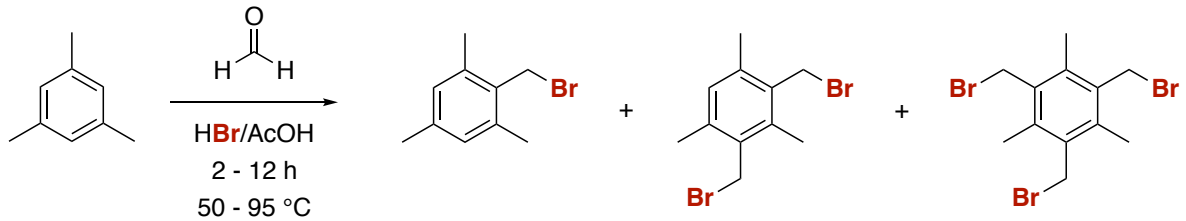

Figure S3. Bromomethylation of mesitylene.[5]

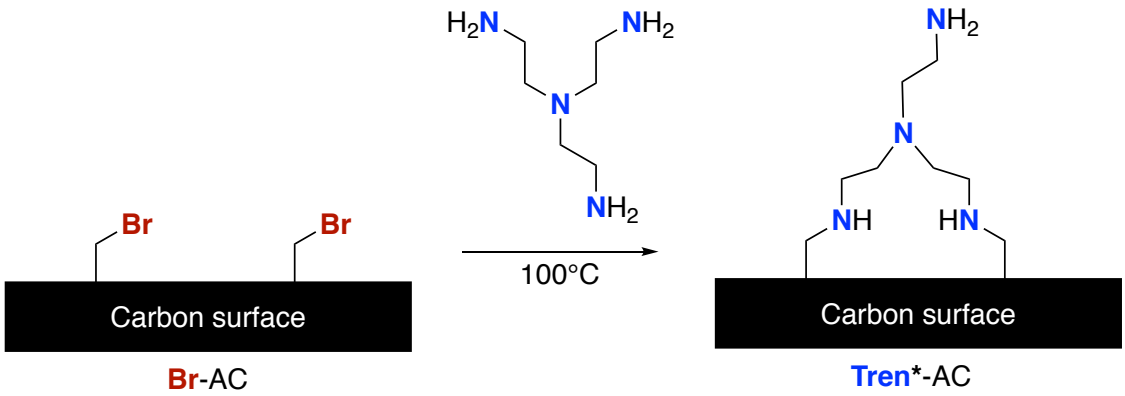

Figure S4. Proposed formation of Tren bridging structures on Br-AC via displacement of two bromides by a single Tren molecule.

Trials for the syntheses of Br-AC, N_3-AC, and Fc-AC

Table S1. Trials for bromomethylation of AC

Trial	Br loading (mmol g^{-1})§	Mass increase (%)
1	1.35	53.8
2	1.24	54.6
3[a, f]	1.10	32.6
4[a, d, f]	1.05	35.5
5	1.25	47.8
6[a]	1.07	51.9
7[a, h]	1.21	41.5
8[b]	1.01	39.1
9	0.84	22.6
10[d]	1.37	48.5
11[g]	1.00	65.8
12[c, e, i]	1.12	45.2
Average ± standard deviation	1.13 ± 0.16	44.9 ± 11.7

§ -Determined by XRF
a -Selected for azide substitution (Table S2).
b -Selected for iodide substitution (Table 2, Entry 1)
c -Selected for All_2NH substitution (Table 2, Entry 2)
d -Selected for EN substitution (Table 2, Entry 3a and b)
e -Selected for Me_3EN substitution (Table 2, Entry 4)
f -Selected for tren substitution (Table 2, Entry 5a and b)
g -Selected for NH_4OH substitution (Table 2, Entry 6)
h -Studied with XPS (Figure 3)
i -Studied with nitrogen-sorption (Figure S6, Table 3)

Table S2.Trials for azide substitution of bromide on Br-AC

Trial	Initial Br loading in Br-AC (mmol g^{-1})§	N_3 loading in N_3-AC (mmol g^{-1})*	Remaining Br in N_3-AC (mmol g^{-1}) §	Remaining Br in N_3-AC (%)	Yield (%)
1	1.07	1.00	0.05	4.7	93.4
2	1.07	0.96	0.06	5.6	89.7
3[a]	1.07	0.86	0.07	6.5	80.4
4	1.07	0.78	0.07	6.5	72.9
5	1.10	0.81	0.08	7.3	73.6
6	1.05	0.85	0.07	6.7	81.0
7[a, b]	1.21	1.20	0.10	8.3	99.2
Average ± standard deviation	1.09 ± 0.05	0.92 ± 0.15	0.07 ± 0.02	6.5 ± 1.1	84.3 ± 10.0

* -Determined by EA
§ -Determined by XRF
a -Selected for CuAAC reaction with ethynylferrocene (Table S3).
b -Studied with XPS (Figure 5)

Table S3. Trials for CuACC coupling of ethynthylferrocene to N_3-AC to form Fc-AC

Trial	Initial Br loading in Br-AC (mmol g^{-1})§	N_3 loading in N_3-AC (mmol g^{-1})*	Triazole loading in Fc-AC (mmol g^{-1})*	Fe loading in Fc-AC§ (mmol g^{-1})§	Yield from N_3-AC (%)	Yield from Br-AC (%)
1	1.07	0.86	0.77	0.78	90.7	72.9
2[a]	1.21	1.20	1.03	1.02	85.0	84.3
Average ± standard deviation	1.14 ± 0.10	1.03 ± 0.24	0.90 ± 0.18	0.90 ± 0.17	88.5 ± 4.0	78.6 ± 8.1

* -Determined by EA
§ -Determined by XRF
a -Studied with XPS (Figure 8)
Note: Trials 1 and 2 had copper loadings of 0.01 and 0.02 mmol g^{-1}, respectively, as determined by XRF.

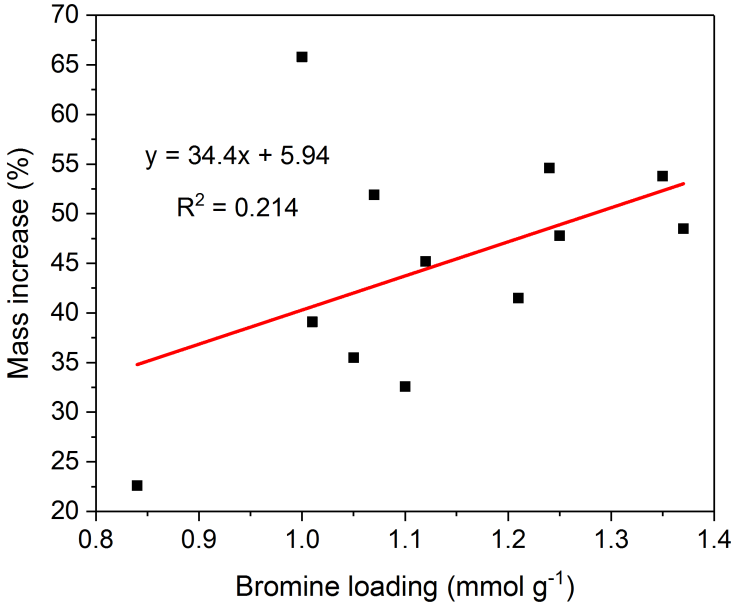

Figure S5. Correlation of the Br-AC bromine loading to its increase in the mass relative to AC.

Bromomethylation of other carbon materials

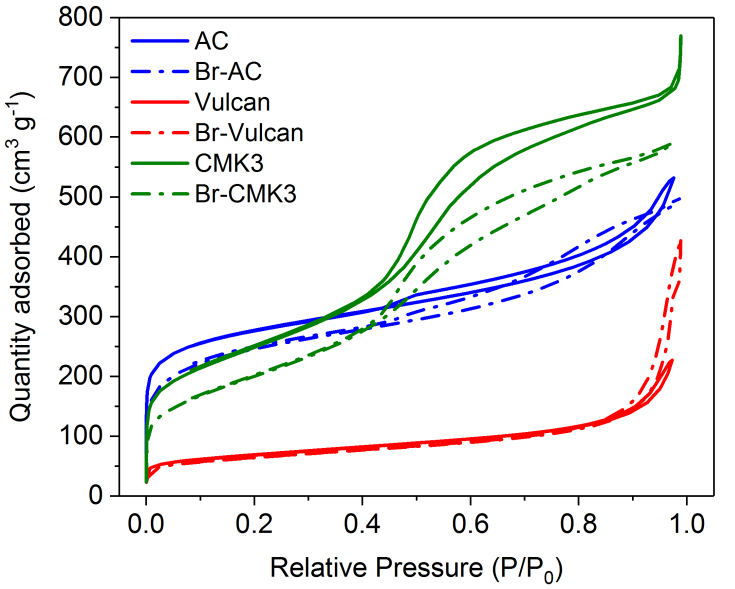

Figure S6. Nitrogen-sorption isotherms for AC, Vulcan, and CMK3 and their bromomethylated derivatives.

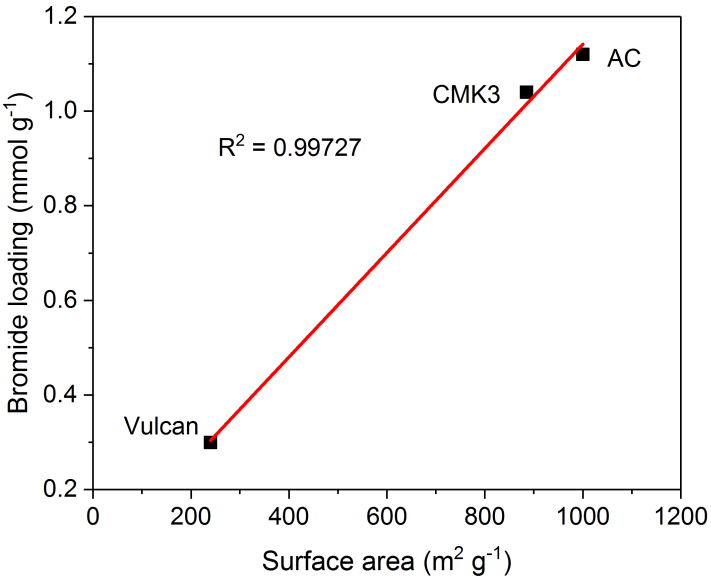

Figure S7. Correlation between bromine loadings and surface area for bromomethylated carbons.

Elemental analysis and X-ray fluorescence of functionalized CMK3 for Li-S batteries

Table S4. X-ray fluorescence of functionalized CMK3.

Sample	Bromine (mmol g^{-1})
CMK3	0
Br-CMK3	0.60
EN-CMK3	<0.1

Table S5. Elemental analysis of functionalized CMK3.

Sample	Nitrogen (mmol g^{-1})
CMK3	0.04*
Br-CMK3	0.05*
EN-CMK3	1.60§

*Concentration below detection limit

§ Corresponds to an EN loading of 0.80 mmol g^{-1}.

X-ray photoelectron spectroscopy of functionalized CMK3 for Li-S batteries

The surface elemental compositions of the three carbons were studied by XPS (Table S6). Br-CMK3, as expected, exhibits a strong bromine signal with an intense feature centered at 70.5 eV (Figure S8, left), similar to the corresponding peak for Br-AC (Figure 3), but with a shoulder at lower binding energies. This could signify the presence of anionic bromide within Br-CMK3.[6, 7] After EN substitution, the bromine content is negligible with a corresponding increase in the nitrogen signal at *ca.* 400 eV (Figure S8, right), corroborating the EA and XRF findings.

Table S6. X-ray photoelectron spectroscopy of functionalized CMK3. Units are atomic %.

Sample	C 1s	N 1s	O 1s	Br 3d
CMK3	95.98	0	4.02	0
Br-CMK3	91.95	0	7.74	0.32
EN-CMK3	94.66	1.32	4.01	0

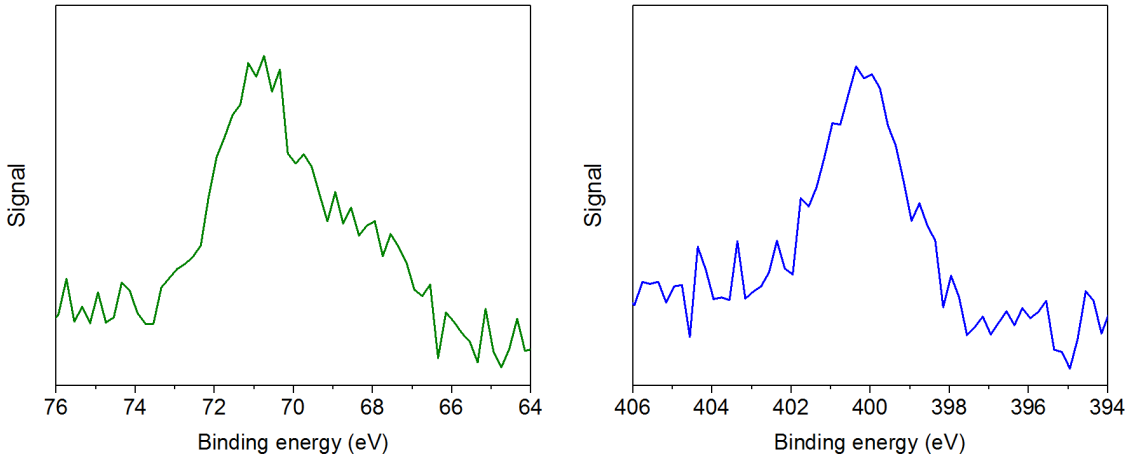

Figure S8. X-ray photoelectron spectra of Br-CMK3 (Br 3d region, left) and EN-CMK3 (N 1s region, right).

Interestingly, the surface oxygen level increases by nearly 2x from CMK3 to Br-CMK3, but then decreases by the same factor upon forming EN-CMK3. A direct comparison of the O 1s signals (Figure S9) shows a larger peak for Br-CMK3 with more intensity at lower binding energies relative to both CMK3 and EN-CMK3. The peak maximum is also shifted accordingly by about 1 eV. Since lower binding energies are known for C-O double bonds compared to single bonds by 1-2 eV,[8] these changes in the O 1s peak suggest more carbonyl groups on the Br-CMK3 surface. A possible explanation could be that the strongly acidic conditions of bromomethylation and/or adventitious dioxygen (O_2) in the HBr/AcOH solvent help to generate more carbonyl groups on Br-CMK3. Surface oxygenation of Br-CMK3 could also be increased during the aerobic work-up steps. In the next reaction, EN couples to these carbonyl groups, liberating water and lowering the oxygen content (*i.e.* an imine condensation). Overall, the changes in the O 1s peak could help explain the high yield of EN-CMK3.

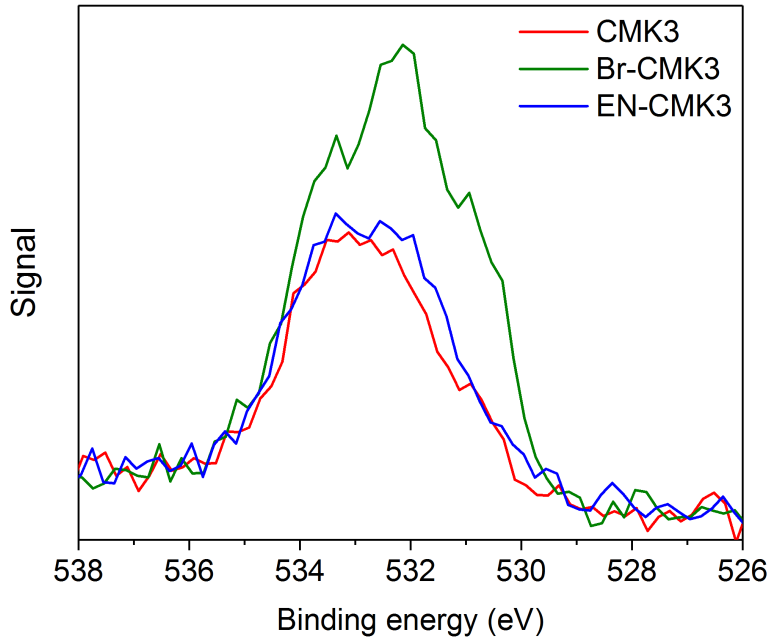

Figure S9. X-ray photoelectron spectra of the O 1s region of CMK3, Br-CMK3, and EN-CMK3. The baselines are offset such that they are approximately the same level for a better comparison of the relative signal intensities.

Small-angle X-ray scattering

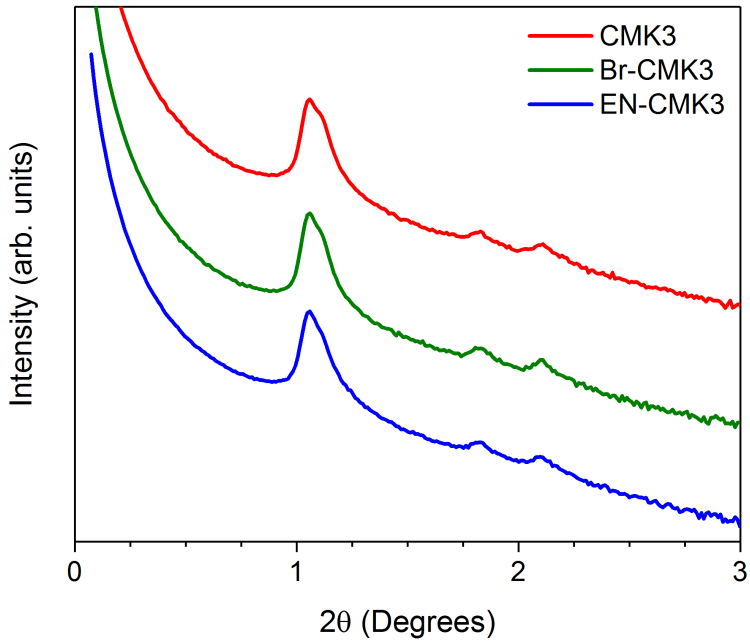

Figure S10. Small angle X-ray scattering patterns for CMK3, Br-CMK3, and EN-CMK3. The intensities are offset for clarity.

X-ray diffraction

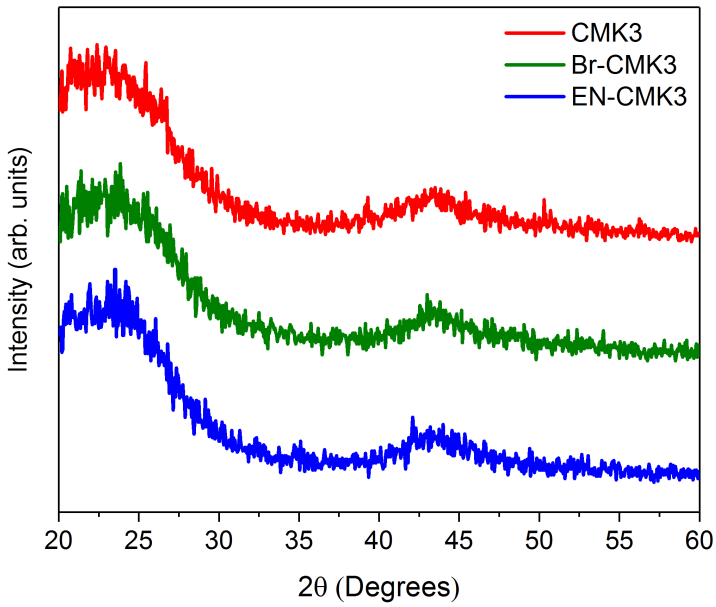

Figure S11. X-ray diffractograms for CMK3, Br-CMK3, and EN-CMK3. The intensities are offset for clarity.

Scanning electron microscopy

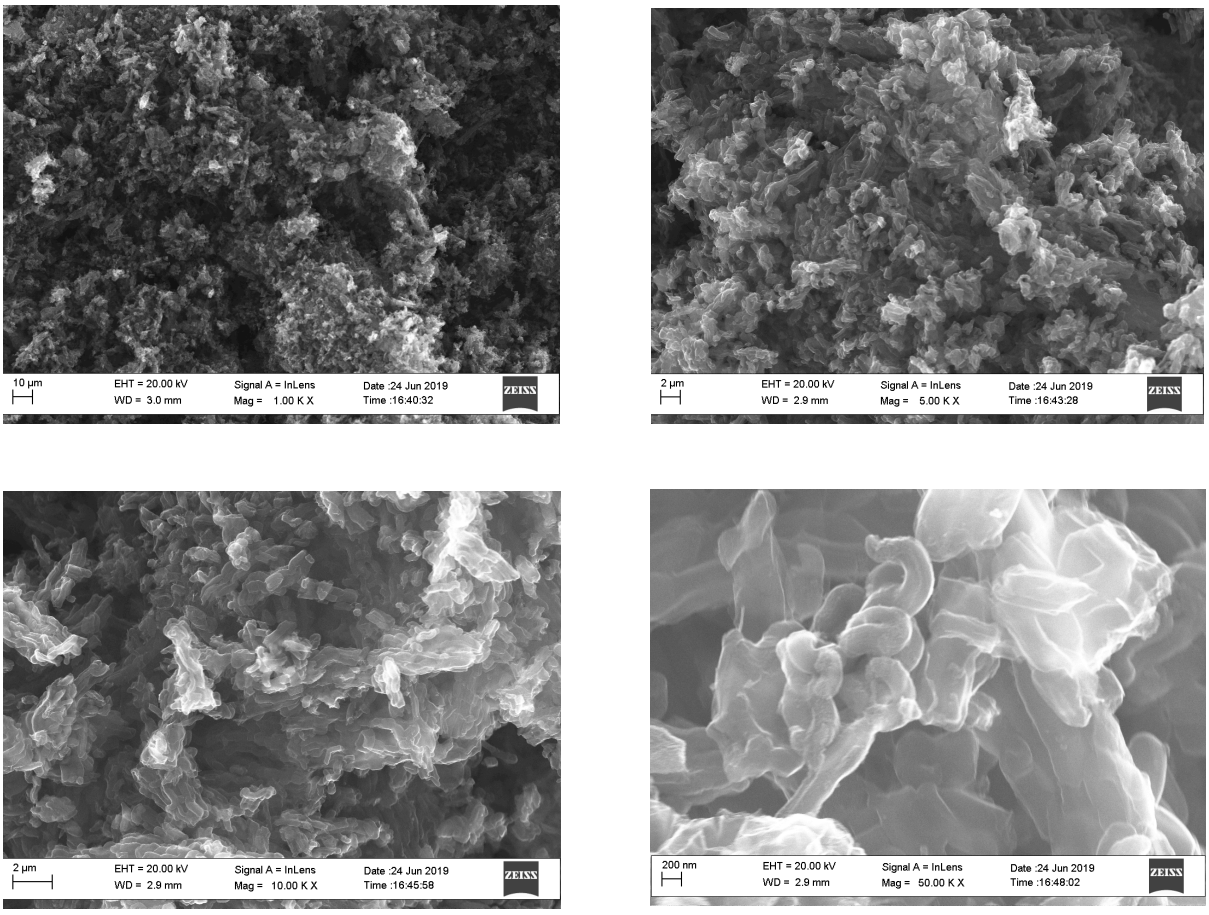

Figure S12. Scanning electron microscopy images of CMK3 at magnifications of 1k (upper left), 5k (upper right), 10k (lower left), and 50k (lower right).

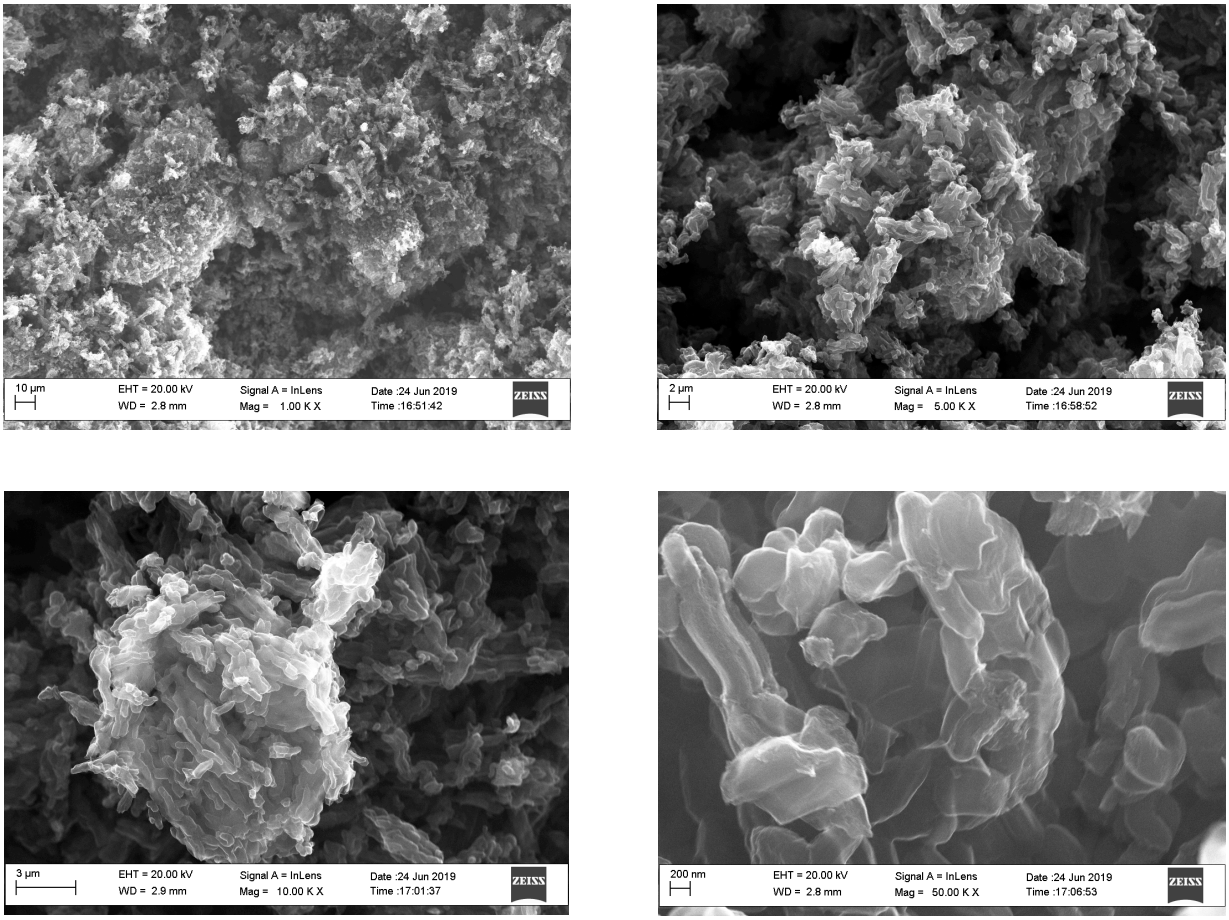

Figure S13. Scanning electron microscopy images of Br-CMK3 at magnifications of 1k (upper left), 5k (upper right), 10k (lower left), and 50k (lower right).

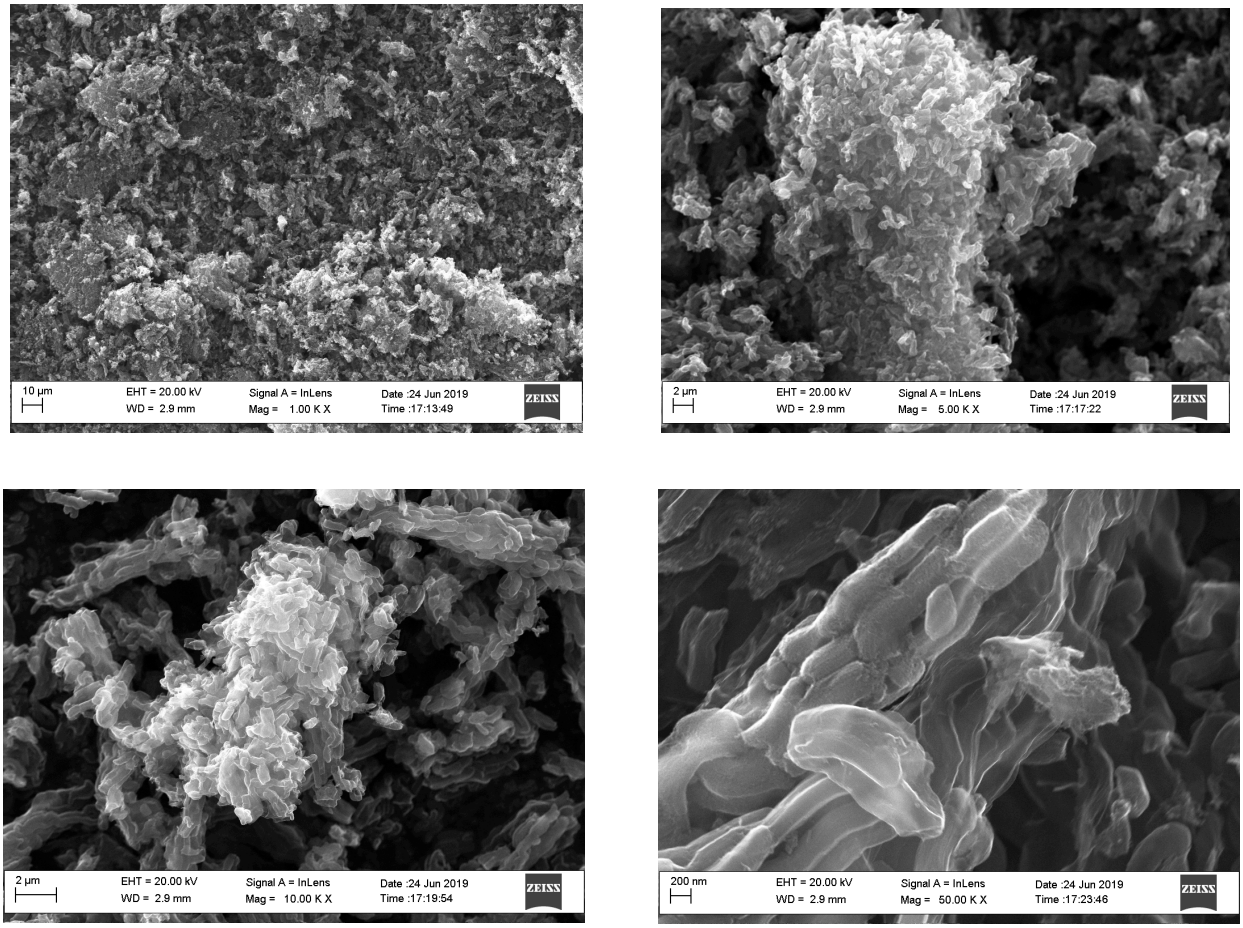

Figure S14. Scanning electron microscopy images of EN-CMK3 at magnifications of 1k (upper left), 5k (upper right), 10k (lower left), and 50k (lower right).

Battery cycling with $LiNO_3$

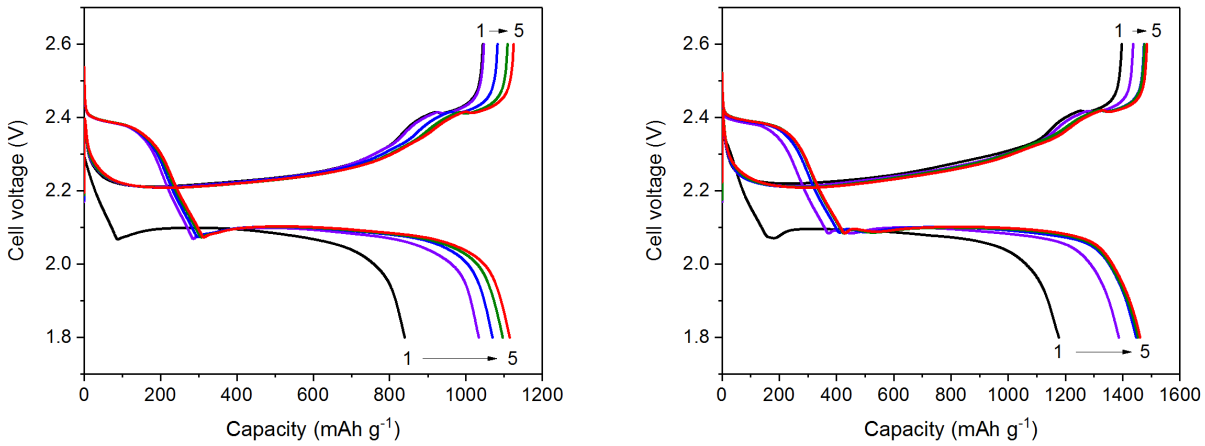

Figure S15. Waveforms at 0.1 C of catholyte/$LiNO_3$ cells for CMK3 (left) and EN-CMK3 (right). The cycles are color coded as follows: 1st black, 2nd violet, 3rd blue, 4th green, and 5th red.

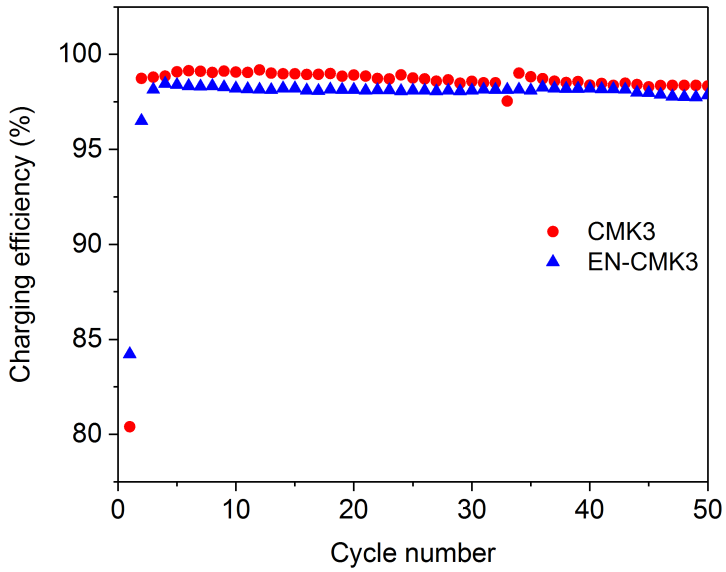

Figure S16. Charging efficiencies at 0.1 C of catholyte/$LiNO_3$ cells with a CMK3 or EN-CMK3 cathode.

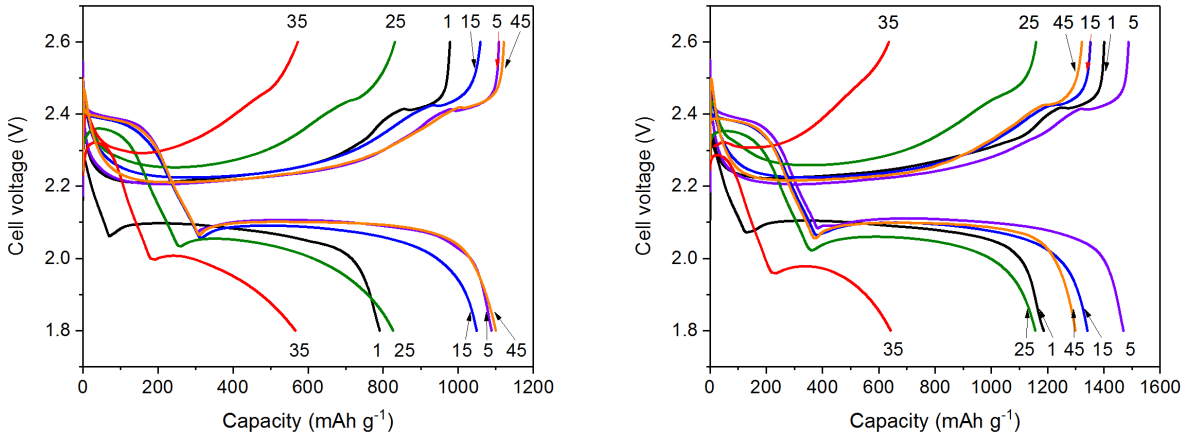

Figure S17. Waveforms of catholyte/$LiNO_3$ cells for rate tested CMK (left) and EN-CMK3 (right). The waveforms are color coded as follows: 1st (0.1C) black, 5th (0.1C) violet, 15th (0.2C) blue, 25th (0.5C) green, 35th (1C) red, and 45th (0.1C) orange.

Battery cycling with LiTFSI

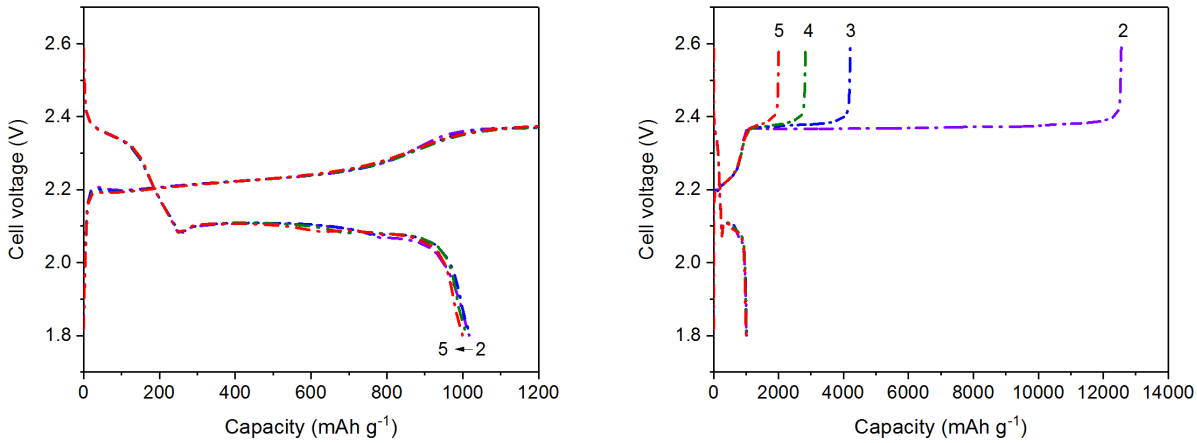

Figure S18. Waveforms at 0.1 C of the catholyte/LiTFSI cell for with a CMK3 cathode. The waveforms are color coded as follows: 2nd violet, 3rd blue, 4th green, and 5th red. The right graph contains the extended version of the left one in order to display the long charging times required.

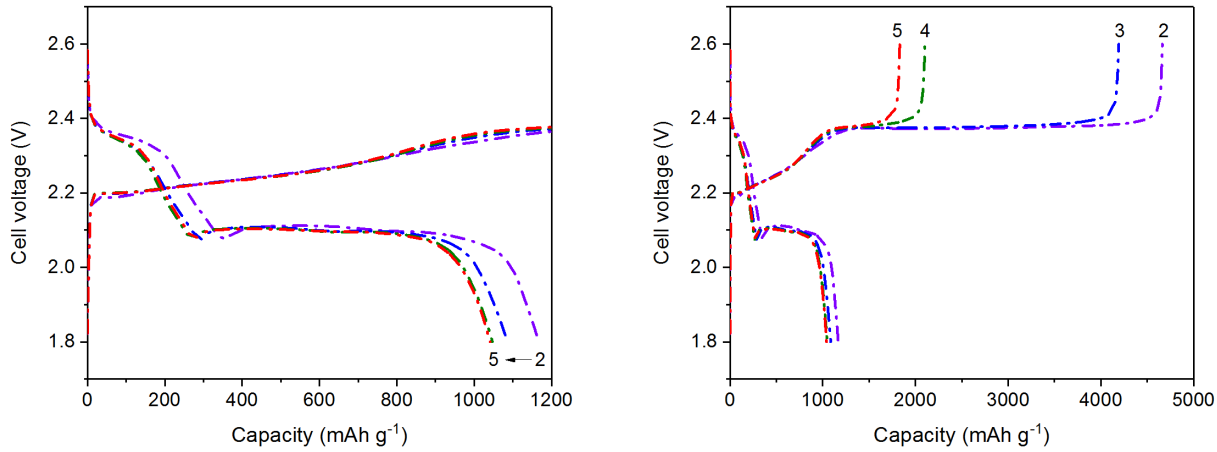

Figure S19. Waveforms at 0.1 C of the catholyte/LiTFSI cell with an EN-CMK3 cathode. The waveforms are color coded as follows: 2nd violet, 3rd blue, 4th green, and 5th red. The right graph contains the extended version of the left one in order to display the long charging times required.

Cyclic voltammetry

Cyclic voltammetry was employed to assess the innate redox activity of the EN surface groups, $LiNO_3$, and LiTFSI and to elucidate their roles in the constant current (CC) cycling studies. The working electrode was either CMK3 or EN-CMK and was paired with variable electrolytes (Table S7).

Table S7. Electrolyte composition for Cyclic Voltammetry Experiments

Electrolyte	Li_2S_8	$LiNO_3$	LiTFSI
1	0	0	1.0
2	0	0.4	1.0
3	0.2	0.4	0
4	0.2	0	0.4

Voltage limits: 1.8 to 2.6 V vs. Li/Li$^+$; scan rate: 50 μV s^{-1}; solvent: 1:1 DOL-DME; all concentrations are molar.

The native carbon oxide layer of CMK3 and the surface-bonded EN groups of EN-CMK3 with a 1 M electrolytic solution of LiTFSI show negligible redox activity beyond their charging capacities (Table S7, Entry 1; Figure S20, dotted traces); the native oxide layer, EN groups, and TFSI anions are all redox inactive under these conditions and potentials. The addition of 0.4 M $LiNO_3$ introduces an irreversible reduction peak below 2.0 V, which is ascribed to nitrate reduction (Table S7, Entry 2; Figure S20, solid traces). These results are consistent with previous reports, which also found nitrate reduction at lower potentials.[9, 10] As the reduction peaks using CMK3 or EN-CMK3 appear similar, the EN groups do not appreciably impact nitrate reduction.

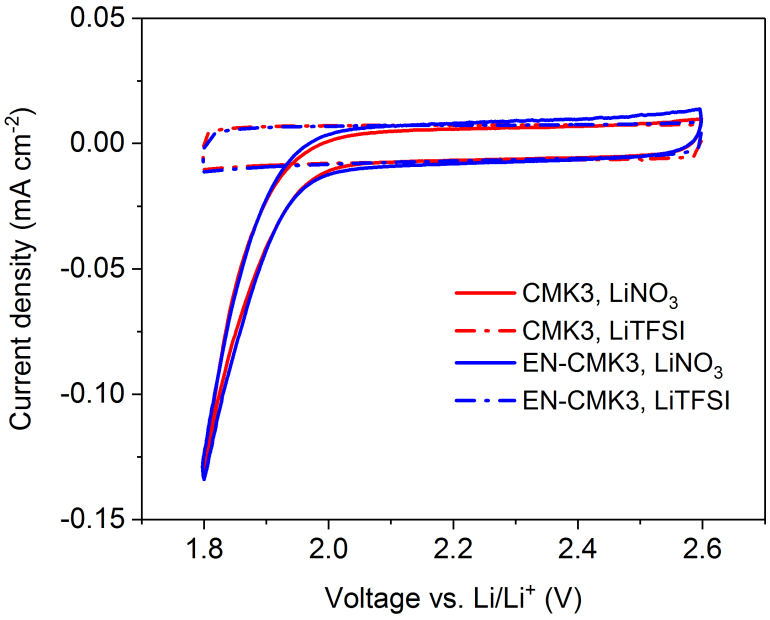

Figure S20. Cyclic voltammograms for CMK3 and EN-CMK3 without polysulfides using electrolyte 1 (1 M LiTFSI, dotted traces) or electrolyte 2 (1 M LiTFSI and 0.4 M $LiNO_3$, solid traces).

Introduction of 0.2 M Li_2S_8 catholyte, with or without nitrate (Table S7, entries 3 and 4), lead to distinctly different CVs (Figure S21). On the cathodic scan, all voltammograms exhibit a smaller reduction feature at *ca.* 2.4 V and a larger feature at 2.0 V, which correspond to the reductions of S_8 and Li_2S_8, respectively.[11, 12] The similarity in voltages indicates that neither nitrate nor the EN groups impact sulfur reduction mechanism during discharge, but the comparatively larger area of the peak at 2.4 V for the $LiNO_3$ cells is consistent with their higher capacities from the CC cycling studies. The anodic scans, on the other hand, reveal a sharp distinction between the two lithium salts. With $LiNO_3$, a large feature centered at 2.4 V with a small shoulder peak at 2.5 V appears. Replacing $LiNO_3$ with LiTFSI results in the main peak splitting into two with the first, larger occurring one at nearly 0.1 V less at 2.3 V and a smaller

one at 2.5 V. Curiously, these changes in the oxidative peaks echo the differences observed in the charging waveforms from the CC studies (Figures 12a and b, S15, S18, and S19). With $LiNO_3$, the voltage increases to 2.4 V before quickly *decreasing* to 2.25 V at about 150 mAh g^{-1}. The voltage also briefly plateaus at 2.4 V before reaching the cut-off voltage of 2.6 V. The long plateau at 2.25 V and short plateau at 2.4 V correspond to the large CV peak at 2.4 V and small shoulder peak 2.5 V, respectively. For comparison, with LiTFSI, the voltage during CC charging starts at a one sloped plateau around 2.25 V until *ca.* 800 mAh g^{-1} before reaching a much longer, flatter plateau at 2.35 V, the latter of which is connected to the LiPS shuttle. For these cells, the voltage never decreases significantly during charging. The CC plateaus at 2.25 V and 2.35 V map onto the CV peaks at 2.3 V and 2.5 V, respectively. The slight differences in voltages between the two techniques are attributable to the different current densities: in the CC studies, the current density at the cathode is 0.23 mA cm^{-2} at 0.1C, which is about an order-of-magnitude less than the peak current density in the CV traces (*ca.* 2 mA cm^{-2}). Overall, the results from both studies reveal that the anion of the lithium salt has a profound impact on the mechanism of charging.

A direct comparison of CMK3 to EN-CMK3 reveals similar traces with two main differences. First, with $LiNO_3$ (Figure S22, left), the reduction peak at 2.4 V is larger in area with a larger maximum current density for EN-CMK3, which correlates to its increased capacity in the CC studies. Second and most importantly, in the CVs with LiTFSI (Figure S22, right), the area of the peak at 2.5 V is significantly smaller for EN-CMK3. Since this peak corresponds to the LiPS shuttle, its diminished intensity suggests an attenuated shuttle mechanism. In fact, the baseline current density for CMK3 with LiTFSI between 2.5 and 2.6 V is relatively high (0.48 mA cm^{-2}) compared to both EN-CMK3 with LiTFSI (0.18 mA cm^{-2}; Figure S22, right) and CMK3 with $LiNO_3$ (0.05 mA cm^{-2}; Figure S21, left). These observations support LiPS shuttle suppression by both the surface EN groups and $LiNO_3$. The larger baseline current density for EN-CMK3 with LiTFSI relative to CMK3 with $LiNO_3$ is also consistent with the former's reduced, but still significant, LiPS shuttle current from the CC cycling studies (Figure S19).

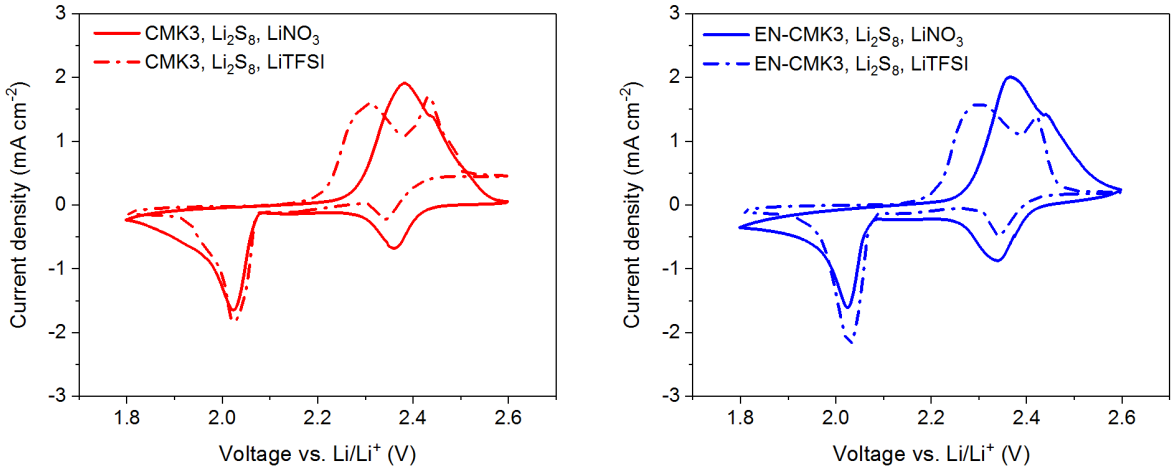

Figure S21. Cyclic voltammograms for CMK3 (red, left) and EN-CMK3 (blue, right) with Li_2S_8 using either electrolyte 3 (with $LiNO_3$, solid traces) or electrolyte 4 (with LiTFSI, dotted traces).

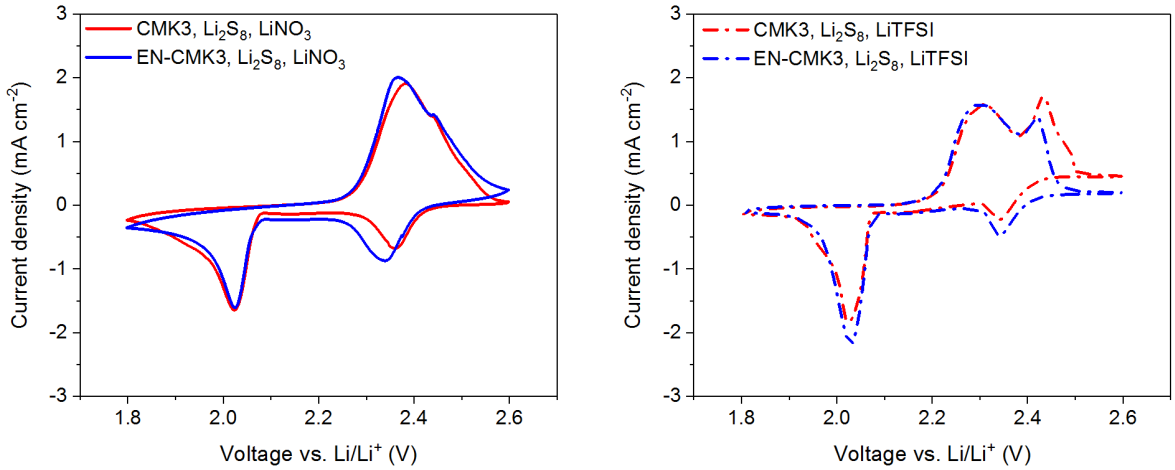

Figure S22. Cyclic voltammograms for CMK3 (red) and EN-CMK3 (blue) with Li_2S_8 using either electrolyte 3 (with $LiNO_3$, solid traces, left) or electrolyte 4 (with LiTFSI, dotted traces, right). All CVs are the same as those in Figure S21, but rearranged to directly compare CMK3 with EN-CMK3.

References

1. A. Devadoss and C. E. D. Chidsey, *J Am Chem Soc*, 2007, **129**, 5370-+.
2. C. C. McCrory, A. Devadoss, X. Ottenwaelder, R. D. Lowe, T. D. Stack and C. E. Chidsey, *J Am Chem Soc*, 2011, **133**, 3696-3699.
3. E. D. Stenehjem, V. R. Ziatdinov, T. D. Stack and C. E. Chidsey, *J Am Chem Soc*, 2013, **135**, 1110-1116.
4. W. D. Samuels, N. H. LaFemina, V. Sukwarotwat, W. Yantasee, X. H. S. Li and G. E. Fryxell, *Separ Sci Technol*, 2010, **45**, 228-235.
5. A. W. Vandermade and R. H. Vandermade, *J Org Chem*, 1993, **58**, 1262-1263.
6. J. Li, L. Vaisman, G. Marom and J. K. Kim, *Carbon*, 2007, **45**, 744-750.
7. X. L. Zhou, S. R. Coon and J. M. White, *The Journal of Chemical Physics*, 1991, **94**, 1613-1625.
8. G. Beamson and D. Briggs, *High Resolution XPS of Organic Polymers: the Scienta ESCA300 Database*, John Wiley and Sons, West Sussex, England, 1992.
9. Z. J. Gong, Q. X. Wu, F. Wang, X. Li, X. P. Fan, H. Yang and Z. K. Luo, *Rsc Adv*, 2016, **6**, 37443-37451.
10. N. Ding, L. Zhou, C. Zhou, D. Geng, J. Yang, S. W. Chien, Z. Liu, M. F. Ng, A. Yu, T. S. Hor, M. B. Sullivan and Y. Zong, *Sci Rep*, 2016, **6**, 33154.
11. L. F. Nazar, M. Cuisinier and Q. Pang, *MRS Bulletin*, 2014, **39**, 436-442.
12. J. H. Kim, T. Kim, Y. C. Jeong, K. Lee, K. T. Park, S. J. Yang and C. R. Park, *Adv Energy Mater*, 2015, **5**, 1500268-n/a.